A&A 536, A53 (2011)
DOI: 10.1051/0004-6361/201015709

Astronomy & Astrophysics

COSMOGRAIL: the COSmological MOnitoring of GRAvItational Lenses⋆,⋆⋆

IX. Time delays, lens dynamics and baryonic fraction in HE 0435-1223

F. Courbin[1], V. Chantry[2,⋆⋆⋆], Y. Revaz[1], D. Sluse[3,⋆⋆⋆⋆], C. Faure[1], M. Tewes[1], E. Eulaers[2], M. Koleva[4,5,6], I. Asfandiyarov[7], S. Dye[8], P. Magain[2], H. van Winckel[9], J. Coles[10], P. Saha[10], M. Ibrahimov[7], and G. Meylan[1]

[1] Laboratoire d'Astrophysique, École Polytechnique Fédérale de Lausanne (EPFL), Observatoire de Sauverny, 1290 Versoix, Switzerland
e-mail: cecile.faure@epfl.ch
[2] Institut d'Astrophysique et de Géophysique, Université de Liège, Allée du 6 Août, 17, 4000 Sart Tilman (Bat. B5C), Liège 1, Belgium
[3] Astronomisches Rechen-Institut am Zentrum für Astronomie der Universität Heidelberg, Mönchhofstrasse 12−14, 69120 Heidelberg, Germany
[4] Université Lyon 1, 69622 Villeurbanne; CRAL, Observatoire de Lyon, 69561 St Genis Laval; CNRS, UMR 5574, France
[5] Instituto de Astrofísica de Canarias, La Laguna, 38200 Tenerife, Spain
[6] Departamento de Astrofísica, Universidad de La Laguna, 38205 La Laguna, Tenerife, Spain
[7] Ulugh Beg Astronomical Institute, Academy of Sciences, Tashkent, Uzbekistan
[8] Cardiff University, School of Physics and Astronomy, Queens Buildings, The Parade, Cardiff, CF24 3AA, UK
[9] Instituut voor Sterrenkunde, Katholieke Universiteit Leuven, Celestijnenlaan 200B, 3001 Heverlee, Belgium
[10] Institute of Theoretical Physics, University of Zürich, Winterthurerstrasse 190, 8057 Zürich, Switzerland

Received 7 September 2010 / Accepted 10 October 2011

ABSTRACT

We present accurate time delays for the quadruply imaged quasar HE 0435-1223. The delays were measured from 575 independent photometric points obtained in the *R*-band between January 2004 and March 2010. With seven years of data, we clearly show that quasar image A is affected by strong microlensing variations and that the time delays are best expressed relative to quasar image B. We measured $\Delta t_{\rm BC} = 7.8 \pm 0.8$ days, $\Delta t_{\rm BD} = -6.5 \pm 0.7$ days and $\Delta t_{\rm CD} = -14.3 \pm 0.8$ days. We spacially deconvolved HST NICMOS2 F160W images to derive accurate astrometry of the quasar images and to infer the light profile of the lensing galaxy. We combined these images with a stellar population fitting of a deep VLT spectrum of the lensing galaxy to estimate the baryonic fraction, $f_{\rm b}$, in the Einstein radius. We measured $f_{\rm b} = 0.65^{+0.13}_{-0.10}$ if the lensing galaxy has a Salpeter IMF and $f_{\rm b} = 0.45^{+0.04}_{-0.07}$ if it has a Kroupa IMF. The spectrum also allowed us to estimate the velocity dispersion of the lensing galaxy, $\sigma_{\rm ap} = 222 \pm 34$ km s^{-1}. We used $f_{\rm b}$ and $\sigma_{\rm ap}$ to constrain an analytical model of the lensing galaxy composed of an Hernquist plus generalized NFW profile. We solved the Jeans equations numerically for the model and explored the parameter space under the additional requirement that the model must predict the correct astrometry for the quasar images. Given the current error bars on $f_{\rm b}$ and $\sigma_{\rm ap}$, we did not constrain H_0 yet with high accuracy, i.e., we found a broad range of models with $\chi^2 < 1$. However, narrowing this range is possible, provided a better velocity dispersion measurement becomes available. In addition, increasing the depth of the current HST imaging data of HE 0435-1223 will allow us to combine our constraints with lens reconstruction techniques that make use of the full Einstein ring that is visible in this object.

Key words. cosmological parameters – gravitational lensing: strong

1. Introduction

To determine the expansion rate of the Universe, H_0, accurately, it is important to scale the extragalactic distance ladder and to measure $w(z)$, the redshift evolution of the dark energy equation of state parameter (e.g., Frieman et al. 2008).

Some of the most popular methods in use to measure H_0 have recently been reviewed (Freedman & Madore 2010). The huge observational and theoretical efforts invested in these measurements have led to random errors between 3% and 10%, depending on the methods. However, all these methods rely at some level on each other and are in the end all based on the same local standard candles. In addition, the accuracy required on H_0 to measure $w(z)$ and H(z) is of the order of 1% (Hu 2005; Riess et al. 2009, 2011). It is therefore of interest (i) to explore methods that are fully independent of any standard candle and (ii) to combine the different methods to further reduce the current error bar on H_0.

⋆ Based on observations made with the 1.2 m Euler Swiss Telescope, the 1.5 m telescope of Maidanak Observatory in Uzbekistan, and with the 1.2 m Mercator Telescope, operated on the island of La Palma by the Flemish Community, at the Spanish Observatorio del Roque de los Muchachos of the Instituto de Astrofísica de Canarias. The NASA/ESA *Hubble* Space Telescope data was obtained from the data archive at the Space Telescope Science Institute, which is operated by AURA, the Association of Universities for Research in Astronomy, Inc., under NASA contract NAS-5-26555.

⋆⋆ Light curves are only available at the CDS via anonymous ftp to cdsarc.u-strasbg.fr (130.79.128.5) or via http://cdsarc.u-strasbg.fr/viz-bin/qcat?J/A+A/536/A53

⋆⋆⋆ Research Fellow, Belgian National Fund for Scientific Research (FNRS).

⋆⋆⋆⋆ Alexander von Humboldt fellow.

Strong gravitational lensing of quasars and the so-called "time delay method" in multiply imaged quasars is independent of the traditional standard candles (Refsdal 1964) and is based on well understood physics: general relativity. However, it requires to measure the time delays from long-term photometric monitoring of the many lensed quasars, which has long been a serious observational limitation. While the attempts to measure accurate time delays have been numerous, only few quasars have been measured with an accuracy close to the percent (e.g., Goicoechea 2002; Fassnacht et al. 2002; Vuissoz et al. 2008). In addition, the lens model necessary to convert time delays into H_0 often remains poorly constrained and hampers a breaking of the degeneracies between the properties of the lensing galaxy and H_0. In recent years, successful attempts have been made to constrain the lens model as much as possible to break these degeneracies (Suyu et al. 2009, 2010).

COSMOGRAIL, the COSmological MOnitoring of GRAvItational Lenses, aims both at measuring precise time delays for a large sample of strongly lensed quasars, and at obtaining and using all necessary observations to constrain the lens models. The present paper describes the COSMOGRAIL results for the quadruply imaged quasar HE 0435-1223, using deep VLT spectra and deconvolved HST images.

HE 0435-1223 (α(2000): 04h38min14.9s; δ(2000) = $-12°17'14.''4$) was discovered by Wisotzki et al. (2000) during the Hamburg/ESO Survey (HES) for bright quasars in the Southern Hemisphere. It was identified two years later as a quadruply imaged quasar by Wisotzki et al. (2002). The redshift of the source is $z_s = 1.689$ (Wisotzki et al. 2000) and that of the lens is $z_l = 0.4546 \pm 0.0002$ (Morgan et al. 2005). The quasar shows evidence for intrinsic variability, which makes it a good candidate for determining the time delays between the different images. The local environment of the lensing galaxy has been studied in detail by Morgan et al. (2005) using the *Hubble* Space Telescope (HST) Advanced Camera for Surveys (ACS) and by Momcheva (2009), who has found that the lensing galaxy lies in a group of at least 11 members. The velocity dispersion of this group is $\sigma \sim 496$ km s^{-1}.

Analytical lens models of HE 0435-1223 are given by Kochanek et al. (2006), who have also measured time delays from two years of optical monitoring: $\Delta t_{AD} = -14.37^{+0.75}_{-0.85}$ days, $\Delta t_{AB} = -8.00^{+0.73}_{-0.82}$ days, and $\Delta t_{AC} = -2.10^{+0.78}_{-0.71}$ days. For a fixed $H_0 = 72 \pm 7$ km s^{-1} Mpc^{-1} they found that the lensing galaxy must have a rising rotation curve at the position of the lensed images and a non-constant mass-to-light ratio. Moreover, high dark matter surface densities are required in the lens halo. New monitoring data of Blackburne & Kochanek (2010) analysed using a physically motivated representation of microlensing give time delays compatible with those of Kochanek et al. (2006), although these authors do not provide their measured values.

2. Photometric monitoring

2.1. Optical imaging

HE 0435-1223 was monitored during more than six years, from January 2004 to March 2010, through the *R* filter, using three different telescopes: the Swiss 1.2 m Euler telescope located on the ESO La Silla site (Chile), the Belgian-Swiss 1.2 m Mercator telescope located at the Roque de Los Muchachos Observatory, La Palma, Canary Island (Spain), and the 1.5 m telescope located at the Maidanak Observatory (Uzbekistan). In addition we also use 136 epochs from the two-year long monitoring of Kochanek et al. (2006), from August 2003 to April 2005, obtained with the ANDICAM camera mounted on the 1.3 m Small and Moderate Aperture Research Telescope System (SMARTS) located at the Cerro Tololo Inter-American Observatory (CTIO) in Chile. A summary of the observations is given in Table 1. Note that we used the published photometry for the SMARTS data, i.e., we did not reprocess the original data frames with our own photometric pipeline.

2.2. Image processing and deconvolution photometry

The data from the three telescopes used by the COSMOGRAIL collaboration are analysed with the semi-automated reduction pipeline described in Vuissoz et al. (2007). The main challenge was that we had to assemble data from different telescopes: each camera has a different size, resolution and orientation on the plane of sky.

The pre-reduction for each observing epoch consists of flat-fielding using master sky-flats. The Euler image with the best seeing was taken as the reference frame to register all other frames. This reference frame was taken on the night of November 11, 2005 and has a seeing of $0.''82$. Two reference stars were then chosen in the field of view (Fig. 1) to compute the geometrical transformations between the images. This transformation involves a spatial scaling and a rotation. The reference stars were also used to compute the relative photometric scaling between the frames taken at different epochs. Eventually, the L. A. Cosmic algorithm (van Dokkum 2001) was applied separately to every frame to remove cosmic rays. All images were checked visually to make sure that no pixel was removed inappropriately, especially in the frames with good seeing.

The photometric measurements were carried out using "deconvolution photometry" with the MCS deconvolution algorithm (Magain et al. 1998). This software has been successfully applied to a variety of astrophysical problems ranging from gravitationally lensed quasars (e.g., Burud et al. 2000, 2002) to the study of quasar host galaxies (e.g., Letawe et al. 2008), or to the search for extrasolar planets using the transit technique (e.g., Gillon et al. 2007a,b). Image deconvolution requires accurate knowledge of the instrumental and atmospheric point spread function (PSF). The latter was computed for each frame from the four stars labelled PSF 1-4 in Fig. 1. These stars are from 0 to 1 mag brighter than the quasar images in HE 0435-1223 and are located within $2'$ from the centre of the field, which minimizes PSF distortions.

Because it does not attempt to achieve an infinitely high spatial resolution, the MCS algorithm produces deconvolved images that are always compatible with the sampling theorem. This avoids deconvolution artefacts and allowed us to carry out accurate photometry over the entire field of view. Moreover, the deconvolved image was computed as the sum of extended numerical structures and of analytical point sources whose shape is chosen to be symmetrical Gaussians. In the case of gravitationally lensed quasars, the numerical channel of this decomposition contains the lensing galaxy. The photometry and astrometry of the quasar images were returned as a list of intensities and positions of Gaussian deconvolved profiles. Finally, the deconvolved image can be computed on a grid of pixels of arbitrary size. In the present work, the pixel size in the deconvolved frames is half the pixel size of the Euler data, i.e., $0.''172$. The spatial resolution in the deconvolved frames is two pixels full-width-at-half-maximum (FWHM), i.e., $0.''35$.

With the MCS software, dithered images of a given target can be "simultaneously deconvolved" and combined into a single deep and sharp frame that matches the whole dataset at once,

Table 1. Summary of the optical monitoring data.

Telescope	Camera	FoV	Pixel	Period of observation	#obs.	Exp. time	Seeing	Sampling
Euler	C2	$11' \times 11'$	$0\farcs344$	Jan. 2004–Mar. 2010	301	5×360 s	$1\farcs37$	6 days
Mercator	MEROPE	$6.5' \times 6.5'$	$0\farcs190$	Sep. 2004–Dec. 2008	104	5×360 s	$1\farcs59$	11 days
Maidanak	SITE	$8.9' \times 3.5'$	$0\farcs266$	Oct. 2004–Jul. 2006	26	10×180 s	$1\farcs31$	16 days
Maidanak	SI	$18.1' \times 18.1'$	$0\farcs266$	Aug. 2006–Jan. 2007	8	6×300 s	$1\farcs31$	16 days
SMARTS	ANDICAM	$10' \times 10'$	$0\farcs300$	Aug. 2003–Apr. 2005	136	3×300 s	$\leq 1\farcs80$	4 days
TOTAL	–	–	–	Aug. 2003–Mar. 2010	575	242.5 h	–	3.2 days

Notes. The temporal sampling is the mean number of days between two consecutive observations.

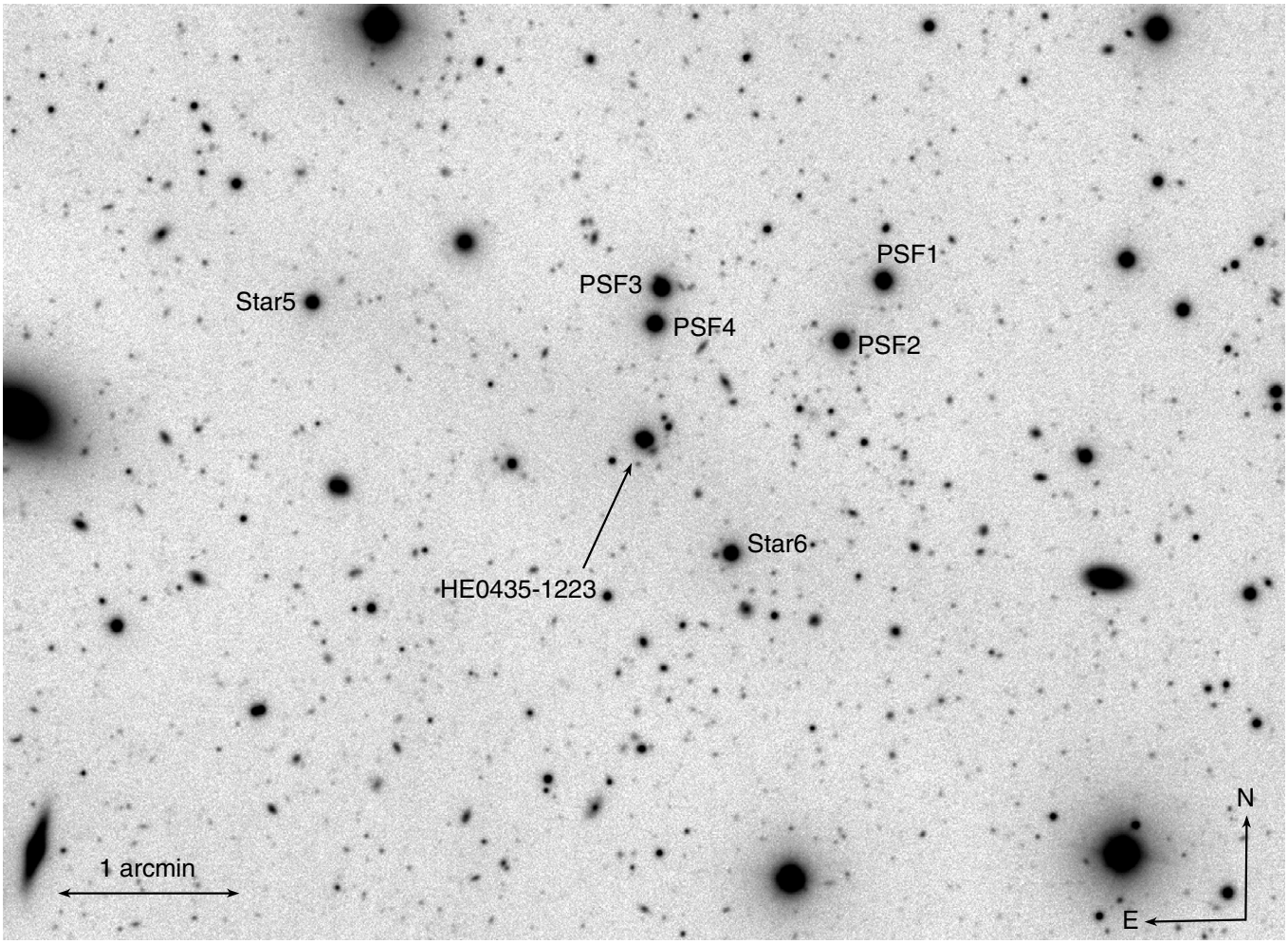

Fig. 1. Part of the field of view of the 1.2 m Swiss Euler telescope, with HE 0435-1223 visible in the centre. The four PSF stars used for deconvolution purposes and the two reference stars used to carry out the flux calibration are indicated.

given the PSFs and the noise maps of the individual frames. In doing this, the intensities of the point sources are allowed to vary from one frame to the next while the smooth background, which includes the lensing galaxy, is held constant in all frames. The result of the process is shown in Fig. 2, where the point sources are labelled as in Wisotzki et al. (2002). Prior information on the object to be deconvolved can be used to achieve the best possible results. In the case of HE 0435-1223 the relative positions of the point sources are fixed to the HST astrometry obtained in Sect. 3.

Figure 3 shows the deconvolution light curves obtained for each quasar image of HE 0435-1223, where the 1σ error bars account both for the statistical and systematic errors. The statistical part of the error was taken as the dispersion between the photometric points taken during each night. The systematic errors were estimated by carrying out the simultaneous deconvolution of reference stars in the vicinity of HE 0435-1223.

Finally, a small scaling factor was applied to the light curves of all telescopes, including the published light curves of Kochanek et al. (2006), to match the Euler photometry. These shifts are all smaller than 0.03 mag.

3. HST NICMOS2 imaging

We used deep near-IR HST images of HE 0435-1223 to derive the best possible relative astrometry between the quasar

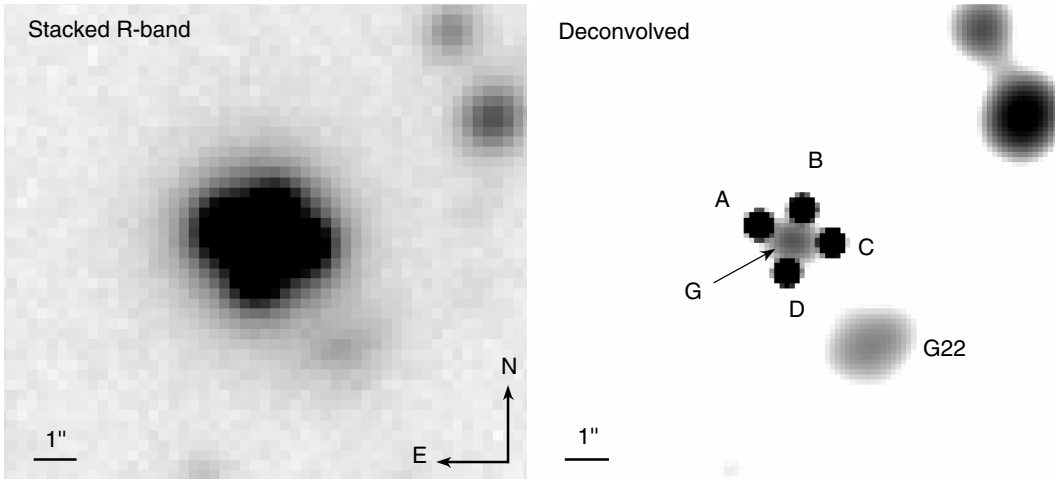

Fig. 2. Result from the simultaneous deconvolution of the ground-based frames. G is the lensing galaxy and G22 (Morgan et al. 2005) is its closest neighbour on the plane of the sky. The grey scale in the deconvolved image is set to display all light level above $3 \times \sigma_{\rm sky}$. The FWHM resolution of the deconvolved image is 0.″34.

images and the lensing galaxy and to constrain the light distribution in the lensing galaxy. The data are part of the CASTLES project (Cfa-Arizona Space Telescope LEns Survey) and were acquired in October 2004 (PI: C. S. Kochanek) with the camera 2 of NICMOS, the Near-Infrared Camera and Multi-Object Spectrometer. They consist of four dithered frames taken through the *F160W* filter (*H*-band) in the MULTIACCUM mode with 19 samples and calibrated by CALNICA, the HST image reduction pipeline. The total exposure time amounts to approximately 44 min and the pixel scale is 0.″075652.

The MCS deconvolution algorithm was used to combine the four NIC2 frames into a deep sharp IR image. We followed the iterative technique described in Chantry et al. (2010) and Chantry & Magain (2007), which allowed us to build a PSF in the absence of a stellar image in the field of view. The method can be summarised as follows. First, we estimated the PSF using `Tiny Tim` software (Krist & Hook 2004) and carried out the simultaneous deconvolution of the four F160W frames using a modified version of the MCS software (Magain et al. 2007). This produces a first approximation of the extended channel of the deconvolved image, i.e., the lensing galaxy and the lensed quasar host galaxy. We reconvolved the latter by the PSF and subtracted it from the original data. A new estimate of the PSF was built on the new image that now contained only the quasar images. The process was repeated until the residual image was satisfactory (for more details see Chantry et al. 2010). Figure 4 shows the result. In this image the pixel size is half that of the original data and the resolution 0.″075 (FWHM), unveiling an almost full Einstein ring.

In the final deconvolved image, the lensing galaxy was modelled analytically rather than numerically to minimise the number of degrees of freedom. We found that the best-fit profile is an elliptical de Vaucouleurs with the parameters as given in Table 3. The astrometry of the quasar images relative to the lensing galaxy, corrected for the known distortions of the NIC2 camera and for the difference of pixel scale between the x and y directions is summarised in Table 2. Based on our previous work using deconvolution of NICMOS images (Chantry & Magain 2007), we estimate that the total error bars, accounting for residual correction of the distortions amounts to 2 mas. Our results agree well with previous measurements from HST/ACS (Morgan et al. 2005) or HST/NIC2 imaging (Kochanek et al. 2006), also shown for comparison in Table 2.

4. Time delay measurement

4.1. Curve shifting method

Our method to measure the time delays is based on the dispersion technique of Pelt et al. (1996): the light curves are shifted in time and in magnitude to minimise a global dispersion function. In addition, the light curves are distorted on long time scales to account for slow microlensing variations. This was made by adding low-order polynomials to either the full curves or to specific observing seasons.

Pelt et al. (1996) has defined several dispersion statistics between pairs of light curves. We implemented a dispersion estimate similar to D_3^2 (see Eq. (8) of Pelt et al. 1996), which performed a linear interpolation between points of one of the curves over a maximum range of 30 days. In the case of four light curves, we defined a total dispersion that is the sum of the dispersions computed using the 12 possible permutations of two curves among four. Each pair was considered twice so to avoid the arbitrary choice of a reference light curve. The photometric error bars were taken into account to weight the influence of the data points in the dispersion. We then minimised the total dispersion by modifying the time delays and the microlensing polynomials.

4.2. Microlensing and influence on the time delay

Simulated light curves that mimic the observed data were used to estimate the robustness of the method. The error bars on the time delays were calculated using Monte Carlo simulations, i.e., redistributing the magnitudes of the data points according to their photometric error bars. The width of the resulting time delay distributions gives us the 1σ error bars.

Because of microlensing we do not have access to the intrinsic variations of the quasar. We represent microlensing in three of the light curves as a relative variation with respect to the fourth light curve, taken as a reference. We tested each of the four light curves in turn as a reference and kept the one that

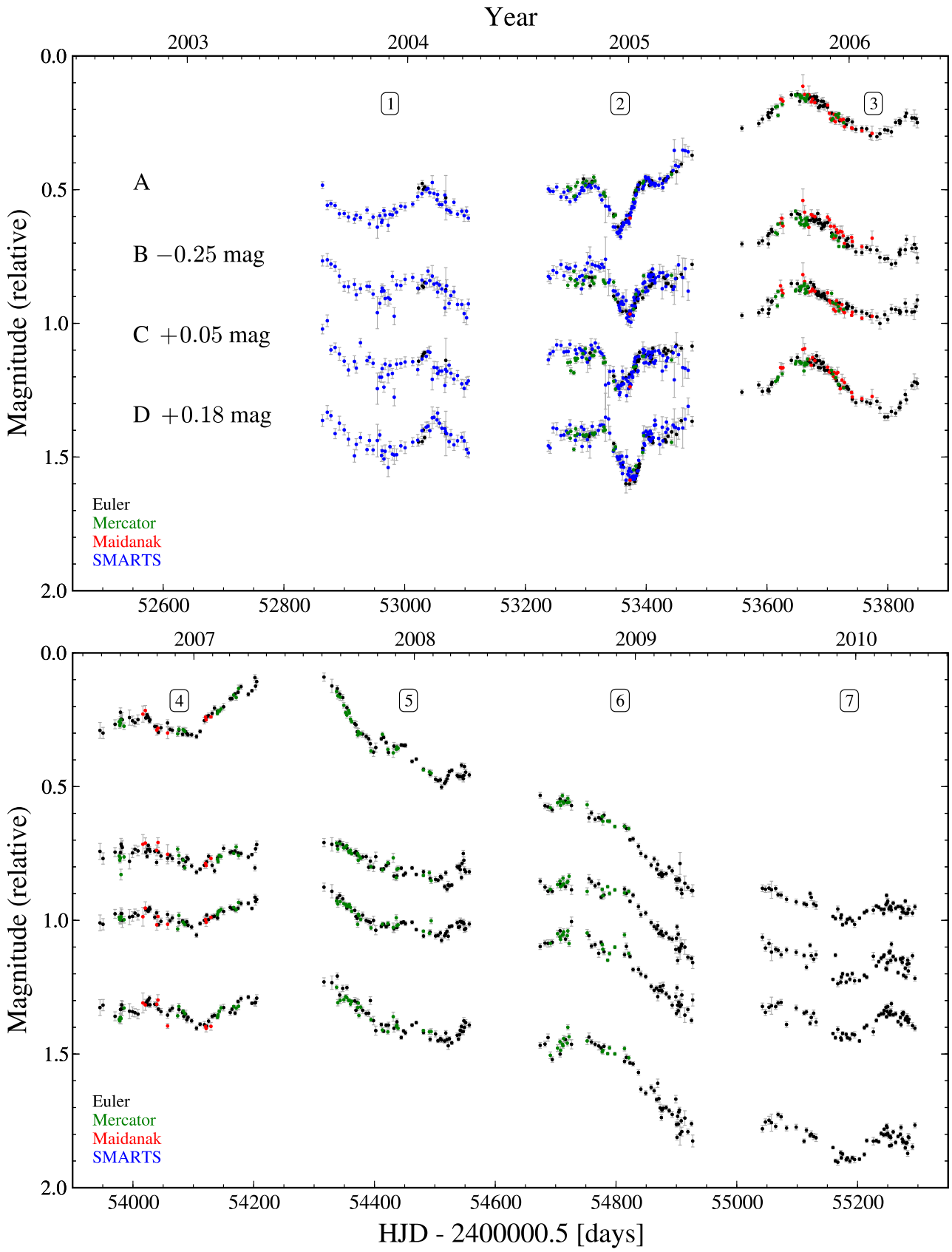

Fig. 3. *R*-band light curves of the four lensed images of HE 0435-1223 from December 2003 to April 2010. The magnitudes are given in relative units as a function of the Heliocentric Julian Day (HJD), along with their total 1σ error bars. These light curves are available in tabular form at the CDS.

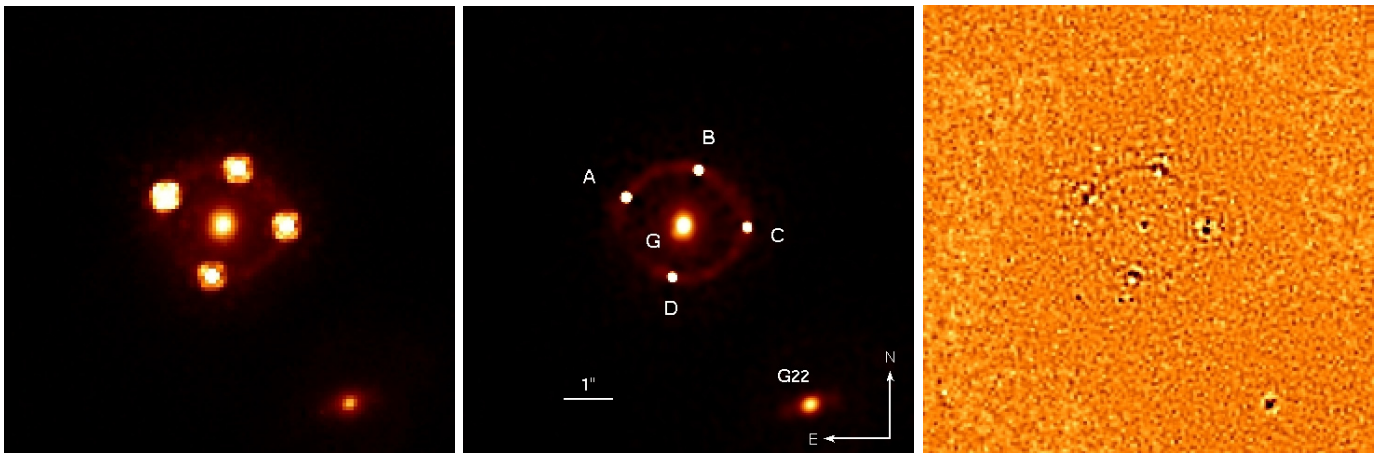

Fig. 4. *Left*: combination of the four original HST/NIC2 F160W frames of HE 0435-1223. The field of view is 9 × 9 arcsec. *Middle*: deconvolved image, where the lensing galaxy is modelled as a de Vaucouleurs profile (see text). The nearest galaxy on the plane of the sky, G22, is also indicated. *Right*: residual map in units of the noise. The colour scale ranges from -4σ (white) to $+4\sigma$ (black).

Table 2. Relative astrometry of HE 0435-1223 as derived from the simultaneous deconvolution of all NIC2 frames.

	This work			Morgan et al. (2005)		Kochanek et al. (2006)	
ID	$\Delta\alpha$ ($''$)	$\Delta\delta$ ($''$)	Mag (F160W)	$\Delta\alpha$ ($''$)	$\Delta\delta$ ($''$)	$\Delta\alpha$ ($''$)	$\Delta\delta$ ($''$)
A	0.	0.	17.20 ± 0.01	0.	0.	0.	0.
B	–1.4743 ± 0.0004	+0.5518 ± 0.0006	17.69 ± 0.01	–1.477 ± 0.002	+0.553 ± 0.002	–1.476 ± 0.003	+0.553 ± 0.001
C	–2.4664 ± 0.0003	–0.6022 ± 0.0013	17.69 ± 0.02	–2.469 ± 0.002	–0.603 ± 0.002	–2.467 ± 0.002	–0.603 ± 0.004
D	–0.9378 ± 0.0005	–1.6160 ± 0.0006	17.95 ± 0.01	–0.938 ± 0.002	–1.615 ± 0.002	–0.939 ± 0.002	–1.614 ± 0.001
G	–1.1706 ± 0.0030	–0.5665 ± 0.0004	16.20 ± 0.12	–1.169 ± 0.002	–0.572 ± 0.002	–1.165 ± 0.002	–0.573 ± 0.002

Notes. The 1σ error bars are the internal errors after deconvolution. Additional 2-mas systematic errors must be added to these (see text). The magnitudes are in the Vega system. For comparison we show the results from Morgan et al. (2005) using HST/ACS images and from Kochanek et al. (2006) using HST/NIC2 images.

Table 3. Shape parameters for the lensing galaxy in HE 0435-1223.

PA (°)	Ellipticity	$a_{\rm eff}$ ($''$)	$b_{\rm eff}$ ($''$)	$r_{\rm eff}$ ($''$)
174.8 (1.7)	0.09 (0.01)	1.57 (0.09)	1.43 (0.08)	1.50 (0.08)

Notes. The position angle (PA) is measured positive east of north. The 1σ error bars (internal errors) are given in parenthesis.

minimised the residual microlensing variations to be modelled in the 3 others. This is best verified with component B as a reference.

With B as a reference light curve, we note that microlensing in C and D remains smooth and can therefore be modelled with a low-order polynomial drawn over the full length of the monitoring. However, A contains higher frequency variations that need to be accounted for in each season individually, as illustrated in Fig. 5. In doing this, we obtain fairly good fits to the light curves, as shown in the residual signal. To quantify the quality of these residuals, we applied the so-called *one-sample runs test of randomness*, a statistical test to estimate whether successive realizations of a random variable are independent or not. In practice the test was applied to a sequence of residuals to decide whether a model is a good representation of the data. For most seasons in our curves the number of runs was between 1σ and 3σ lower than the value expected for independent random residuals. Thus, although our microlensing model is not fully representative of the real signal, the deviations from the data points remain small.

We tested the robustness of our curve-shifting method in several ways. First, we modelled the microlensing variations using polynomial fits of different orders. Second, we fitted these polynomials either across each individual season or across groups of seasons. Finally, we masked the seasons with the worst residual signal (Fig. 5). All these changes had only a negligible impact on the time delay measurements. We note that this is not the case when considering only two or three seasons of data, which shows the importance of a long-term monitoring with good temporal sampling.

4.3. Final results

Our results are summarised in Table 4 and are compared with the previous measurements of Kochanek et al. (2006), who have used pure a polynomial fit to the light curves and two seasons of monitoring. Using the same data but with our modified dispersion technique, we obtained very similar time delays as Kochanek et al. (2006), but larger error bars. We prefer keeping a minimum possible number of degrees of freedom (e.g., in the polynomial order used to represent microlensing), in accordance with the Occam's razor principle, even to the cost of apparently larger formal error bars.

We also note that Kochanek et al. (2006) give their time delays with respect to A, which, with seven seasons of data, turns out to be the most affected by microlensing. As a consequence the error bars on these time delays are dominated by residual microlensing rather than by statistical errors. The time delays used in the rest of our analysis are therefore measured relative to B.

Finally, we used the mean values of our microlensing corrections to estimate the macrolensing *R*-band flux ratios between the four quasar images, assuming that no long-term microlensing

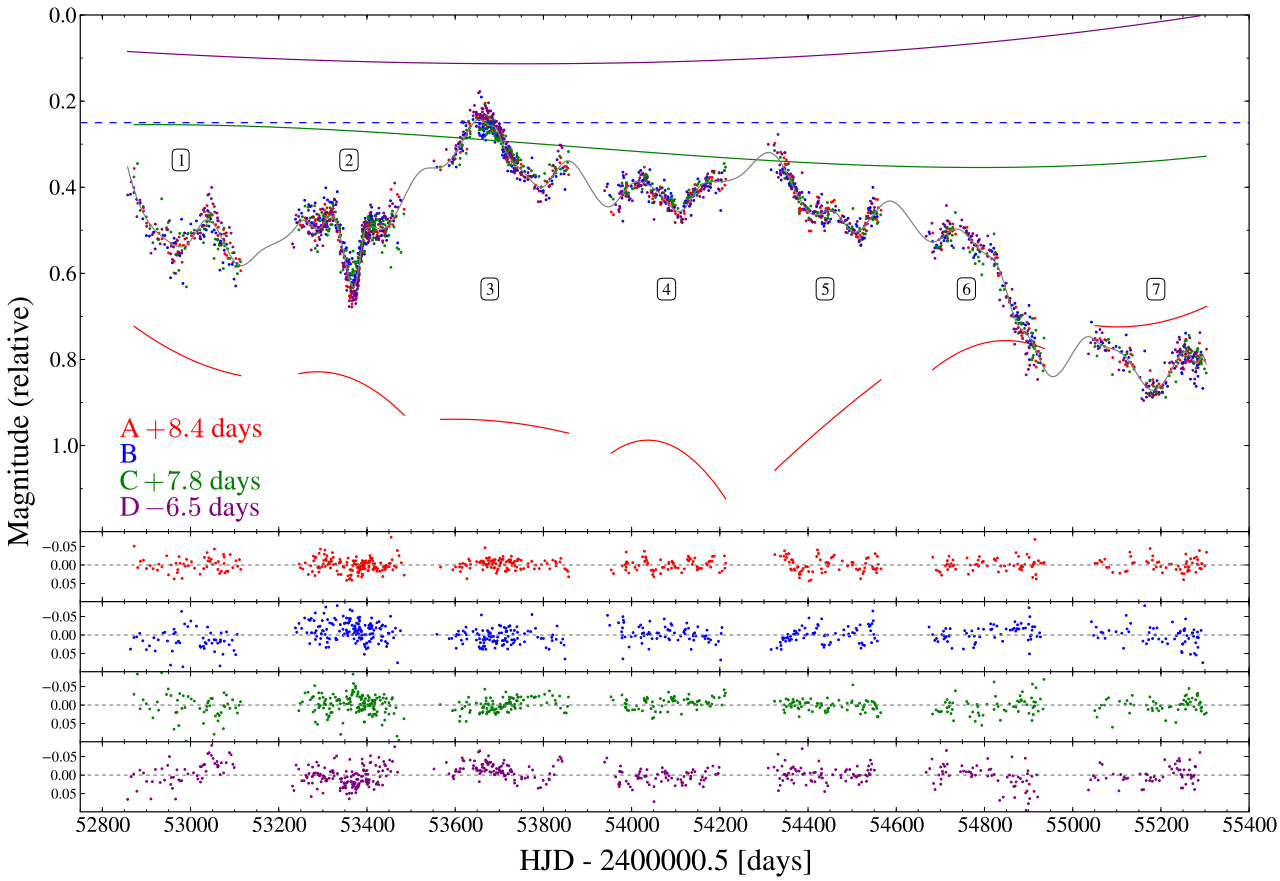

Fig. 5. Light curves obtained with all four telescopes and shifted by time delays of Δt_{BA} = 8.4 days, Δt_{BC} = 7.8 days and Δt_{BD} = −6.5 days. The relative microlensing representations applied on curves A, C and D are shown as continuous curves with respect to the dashed blue line (see text). A fifth-order polynomial was used over the seven seasons to model microlensing on the quasar images C and D, while seven independent third-order polynomials were used for image A. *The lower panels* show residuals obtained by subtracting a simultaneous spline fit (grey) from the light curves.

affects the data. We found $m_B - m_A = \Delta m_{BA} = 0.62 \pm 0.04$, $\Delta m_{BC} = 0.05 \pm 0.01$, and $\Delta m_{BD} = -0.16 \pm 0.01$, which is well compatible with the ratios measured at seven wavelengths by Mosquera et al. (2011). However, these authors report significant wavelength dependence of the image flux ratios, which led us not to use flux ratios as a constraint in the lens models.

5. Constraining the mass profile of the lensing galaxy

The goal of the present section is to constrain the radial mass profile of the lensing galaxy as much as possible, which is the main source of uncertainty on the determination of H_0 with the time delay method. One way of doing this is to use the information contained in the Einstein ring that is formed by the host galaxy of the lensed quasar (Suyu et al. 2010, 2009; Warren & Dye 2003). This works well when a prominent Einstein ring is visible. Unfortunately, given the depth of the current HST images of HE 0435-1223, the radial extent of the ring is too small to efficiently apply this technique. We propose instead to use information on the dynamics and on the stellar mass of the lens, using deep optical spectroscopy.

5.1. Stellar population and velocity dispersion of the lensing galaxy

A deep VLT spectrum of the lensing galaxy is available from Eigenbrod et al. (2006). While the spectrum was originally used to measure the redshift of the galaxy, it turns out to be deep enough ($\langle S/N \rangle \sim 20$) to measure the stellar velocity dispersion and the mass-to-light ratio.

We analysed the data using full spectrum fitting with the ULySS package (Koleva et al. 2009). The method consists in fitting spectra against a grid of stellar population models convolved by a line-of-sight velocity distribution. A single minimisation allowed us to determine the population parameters (age and metallicity) and the kinematics (redshift and velocity dispersion). The stellar mass-to-light ratio was derived from the age and metallicity for the considered model. The simultaneous fit of the kinematical and stellar population parameters reduced the degeneracies between age, metallicity and velocity dispersion (Koleva et al. 2008).

We performed the spectral fit using the PEGASE-HR single stellar population models (SSP, Le Borgne et al. 2004), where the observed flux, F_λ, is modelled as follows:

$$F_\lambda = P_n(\lambda) \times [L(v_{sys}, \sigma) \otimes S(t, [\mathrm{Fe/H}], \lambda)] + Q_m(\lambda). \quad (1)$$

The models were built using the Elodie.3.1 (Prugniel & Soubiran 2001; Prugniel et al. 2007) spectral library and the Kroupa (Kroupa 2001) and Salpeter (Salpeter 1955) initial mass functions (IMF). $L(v_{sys}, \sigma)$ is a Gaussian function of the systematic velocity, v_{sys}, and of the velocity dispersion, σ. $S(t, [\mathrm{Fe/H}], \lambda)$ is the model for the SSP and depends on age and metallicity. P_n is a polynomial of degree n, which models any residual uncertainty in the flux calibration and extinction correction. In addition,

Table 4. Time delays for HE 0435-1223, with the same arrival order convention as Kochanek et al. (2006), i.e., D arrives last.

Data	Method	Δt_{AB}	Δt_{AC}	Δt_{AD}	Δt_{BC}	Δt_{BD}	Δt_{CD}
SMARTS (seasons 1 and 2)	Kochanek (2006)	-8.0 ± 0.8	-2.1 ± 0.8	-14.4 ± 0.8			
SMARTS (seasons 1 and 2)	dispersion	-8.8 ± 2.4	-2.0 ± 2.7	-14.7 ± 2.0	6.8 ± 2.7	-5.9 ± 1.7	-12.7 ± 2.5
COSMOGRAIL (all seasons)	dispersion	-8.4 ± 2.1	-0.6 ± 2.3	-14.9 ± 2.1	7.8 ± 0.8	-6.5 ± 0.7	-14.3 ± 0.8

Table 5. Model parameters of the lens potential well.

$R_{\rm eff}$	8.44 kpc	radius containing 50% of the observed light
$R_{\rm E}$	6.66 kpc	Einstein radius
$f_{\rm b}$	parameter	baryonic fraction in the Einstein radius [0.05−0.5]
$r_\star$	5.3 kpc	stellar component scaling radius
$M_\star$	$M_{\rm h} f_{\rm b}/(1-f_{\rm b})$	stellar total mass
$r_{\star,\rm max}$	$20\,r_\star$	stellar truncation radius
$\gamma_{\rm DM}$	parameter	dark matter inner slope [0−2]
$r_{\rm s}$	parameter	dark matter scaling radius $[1, 2, 4, 8] \times R_{\rm E}$
$M_{\rm h}$	parameter	dark matter total mass $[4.8 \times 10^{11} - 9.1 \times 10^{12}]\ M_\odot$
$r_{\rm s,max}$	$10\,r_{\rm s}$	dark matter truncation radius

Notes. For the variables used as parameters the ranges of values used are given between brackets.

the quasar spectrum might not be perfectly subtracted from the galaxy. To mimic this effect, we included an additive polynomial, Q_m. The order of the additive and multiplicative polynomials is the minimum required to provide an acceptable χ^2, i.e., in our case ($n = 10, p = 1$).

We obtained SSP-equivalent ages and metallicities of $t \sim 3$ Gyr and [Fe/H] ~ 0.0 dex respectively. The corresponding rest-frame B-band stellar mass-to-light ratio is $M_\star/L_B = 3.2^{+0.3}_{-0.5}\ M_\odot/L_{\odot,B}$ using a Kroupa IMF and $M_\star/L_B = 4.6^{+0.9}_{-0.7}\ M_\odot/L_{\odot,B}$ using a Salpeter IMF. The uncertainties in the age and metallicity were estimated via Monte Carlo simulations and propagated in the error in $M_\star/L_B$.

To compute the physical velocity dispersion we subtracted quadratically the instrumental broadening from the measured profile, neglecting the dispersion of the models since they are based on high-resolution templates. The instrumental broadening was measured both from the PSF stars used to carry out the spatial deblending of the spectrum (Eigenbrod et al. 2006) and from the lamp spectra. We obtained the rest-frame physical stellar velocity dispersion of the lensing galaxy: $\sigma_{\rm ap} = 222 \pm 34$ km s^{-1} in an aperture of 1″, i.e., 5.7 kpc.

5.2. Numerical integration of the Jeans equations

In this section we model the lensing galaxy using a 3D spherical potential well formed of two components, one for the stellar part of the mass and one for the dark matter halo. We then perform a numerical integration of the Jeans equations in 3D to predict a theoretical velocity dispersion and a total mass for the model. The assumption of spherical symmetry is sufficient for our purpose, as illustrated by the study of the lensed quasar MG 2016+112, where Koopmans & Treu (2002) introduced an anisotropy parameter and showed that it has almost no influence on the inferred mass slope.

The luminous component of the model is a Hernquist profile (Hernquist 1990):

$$\rho_\star(r) = \frac{\rho_\star(0)}{(r/r_\star)\,(1 + r/r_\star)^3}, \tag{2}$$

where $\rho_\star(0)$ is the central density and $r_\star$ is a scale radius chosen so that the integrated mass in a cylinder of radius $R_{\rm eff}$ (effective radius) is equal to half the total stellar mass $M_\star$. The profile has a maximum radius of $r_{\star,\rm max} = 20\,r_\star$.

The dark matter halo is modelled as a generalised Navarro, Frenk & White (NFW) profile (Navarro et al. 1996):

$$\rho_{\rm h}(r) = \frac{\rho_{\rm h}(0)}{(r/r_{\rm s})^{\gamma_{\rm DM}}(1 + (r/r_{\rm s})^2)^{(3-\gamma_{\rm DM})/2}}, \tag{3}$$

where $\gamma_{\rm DM}$ is the inner slope of the profile, $r_{\rm s}$ is the scaling radius and $\rho_{\rm h}(0)$ is the central mass density. For $\gamma_{\rm DM} = 1$ the model closely follows the standard NFW profile. Its total mass, $M_{\rm h}$, is given in the truncation radius $r_{\rm h,max} = 10\,r_{\rm s}$.

Following the usual convention, the integrated stellar and dark matter masses are related by the baryonic fraction $f_{\rm b}$,

$$f_{\rm b} = \frac{M_\star}{M_{\rm h} + M_\star}. \tag{4}$$

Because all integrations in this work were carried out numerically, $f_{\rm b}$ can easily be computed in any aperture. We chose to compute it in the Einstein radius, which is also where lensing gives the most accurate mass measurement. The velocity dispersion of the stellar component was computed by solving the second moment of the Jeans equation in spherical coordinates (Binney & Merrifield 1998). The velocity dispersion is then

$$\sigma_\star^2(r) = \frac{1}{\rho_\star(r)} \int_r^\infty {\rm d}r'\, \rho_\star(r')\, \partial_{r'}\Phi(r'), \tag{5}$$

where $\Phi(r)$ is the total gravitational potential. Equation (5) is solved numerically as follows. First, the density of each mass component (stars and dark halo) is sampled by N particles, using a Monte-Carlo method. Second, the potential is computed using a *treecode* method (Barnes & Hut 1986). For self-consistency, the density is computed by binning the particles in spherical shells. Then, a velocity is allocated to each particle at a distance r from the galaxy center, following a Gaussian distribution of variance $\sigma_\star(r)$. Finally, the velocity dispersion of the model, $\sigma_{\rm Jeans}$, is computed numerically, by integrating all the particle velocities in an aperture that matches exactly the slit used to carry out the observations.

The advantages of the numerical representation of the lens models are multiple. They allow us (i) to compute velocity

dispersions for any combination of density profiles, even non-parametric ones; (ii) to account for the truncation radius of the halo; (iii) to test the dynamical equilibrium of the system by evolving the model with time. Computing the velocity dispersion as well as the total mass in a cylinder along the line of sight of the observer is then straightforward.

In all calcultations we fixed the effective radius to the one observed for the lensing galaxy, i.e., $R_{\rm eff}$ = 8.44 kpc. The remaining parameter space to explore is composed of the halo scale radius, $r_{\rm s}$, the slope of the profile, $\gamma_{\rm DM}$, and the baryonic fraction, $f_{\rm b}$, within the Einstein radius.

5.3. Applying the dynamical and stellar population constraints

Using our HST photometry, we measured the total rest-frame B-band galaxy luminosity by converting its total H-band magnitude, m_{F160W} = 16.20. Using a k-correction of 1.148, and a galactic extinction[1] of $E(B-V)$ = 0.059 (Schlegel et al. 1998), we find $L_B = 1.04 \times 10^{11}\ L_{B,\odot}$. For a given galaxy model we can therefore compute the total stellar mass-to-light ratio, $M_\star/L_B$, as well as the baryonic fraction that we can compare with the observed ones. This requires a choice of IMF. For a Salpeter IMF we measured $f_{\rm b} = 0.65^{+0.13}_{-0.10}$, while for a Kroupa IMF we measured $f_{\rm b} = 0.45^{+0.04}_{-0.07}$. In our computation of the baryonic fraction, the total mass is the mass in the Einstein radius, $M(<R_{\rm E})$.

We compared the model properties to the data by computing a chi-square, $\chi^2_{\rm Jeans}$. This $\chi^2_{\rm Jeans}$ includes the measured lens velocity dispersion and the total mass in the Einstein radius, $M(<R_{\rm E}) = (3.16 \pm 0.31) \times 10^{11}\ M_\odot$. We allowed for a 10% error on the total mass in the Einstein radius to account for the weak dependence of this mass upon the choice of a lens model, which led to

$$\chi^2_{\rm Jeans} = \left(\frac{\sigma_{\rm Jeans} - 222}{34}\right)^2 + \left(\frac{M(<R_{\rm E}) - 3.16\times10^{11}}{0.31}\right)^2. \quad (6)$$

We used our numerical integration of the Jeans equations to sample the $\gamma_{\rm DM} - f_{\rm b}$ plane, for a given choice of the scale radius, $r_{\rm s}$, of the dark matter halo. Figure 6 shows the value of $\chi^2_{\rm Jeans}$ for 960 000 galaxy models with $r_{\rm s} = 4 \times R_{\rm E} = 25$ kpc. For a given choice of IMF a precise measurement of the baryonic fraction, $f_{\rm b}$, can constrain the dark matter slope γ_{DM} well, at least in the case of a Kroupa IMF.

Figure 6 is drawn for $r_{\rm s} = 4 \times R_{\rm E} = 25$ kpc, which gives the best $\chi^2_{\rm Jeans}$ values. However, models with $\chi^2_{\rm Jeans} < 1$ are also obtained with other values of $r_{\rm s}$. We therefore test the influence of a change in $r_{\rm s}$ by building models for a range of scale radii, $r_{\rm s} = 5, 15, 30$ kpc (i.e., $r_{\rm s} = 0.75\times, 2.25\times, 4.50 \times R_{\rm E}$). Figure 7 summarises the results and shows no influence of $r_{\rm s}$ on the $\gamma_{\rm DM} - f_{\rm b}$ relation unless $r_{\rm s}$ becomes unrealistically small.

The Hernquist profile in our model also has a scale parameter, $r_\star$, which is fixed to the observed value of the effective radius, $R_{\rm eff}$ = 8.44 kpc. Although we have HST images that allow us to measure $R_{\rm eff}$ and although our error bars on this parameter are small, we note that studies of lensing galaxies by different authors often find different $R_{\rm eff}$ values from the same data. This is because different methods are used to subtract the quasar images and to mask (or not) the Einstein ring. We therefore computed models for a range of different $R_{\rm eff}$ and show the influence on the $\gamma_{\rm DM} - f_{\rm b}$ plane in Fig. 8, for $R_{\rm eff} = 4.22, 8.44, 12.88$ kpc.

[1] A galactic extinction calculator is available at this address: http://nedwww.ipac.caltech.edu/forms/calculator.html

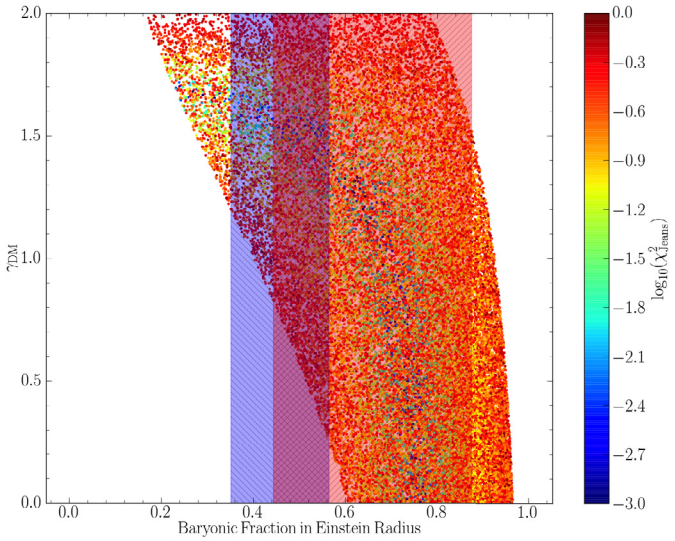

Fig. 6. Radial slope, $\gamma_{\rm DM}$, of the dark matter halo as a function of the baryonic fraction in the Einstein radius, $R_{\rm E}$. The colour code represents the value of $\chi^2_{\rm Jeans}$ for all acceptable models, i.e., $\chi^2_{\rm Jeans} < 1$ (see text; Eq. (6)). The observational limits drawn on $f_{\rm b}$ using our spectrum of the lensing galaxy are indicated as shaded vertical regions. The blue region corresponds to a Kroupa IMF and the red regions corresponds to a Salpeter IMF. In this figure, all models have $r_{\rm s} = 4 \times R_{\rm E} = 25$ kpc.

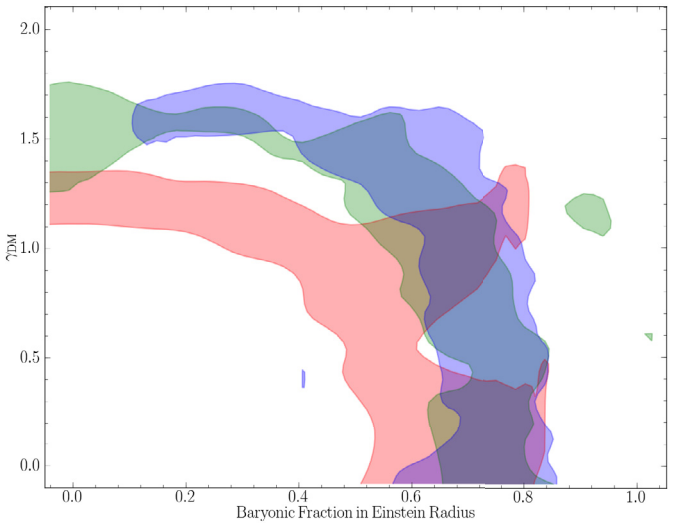

Fig. 7. Effect of change in $r_{\rm s}$, the scale radius of the dark matter halo, on the $\gamma_{\rm DM} - f_{\rm b}$ relation. The contours show the region containing 68% of the models. The blue area has $r_{\rm s} = 25$ kpc (our adopted choice for the final modelling), the green region has $r_{\rm s} = 15$ kpc, and the red region is for models with small scale radii, $r_{\rm s} = 5$ kpc.

This reflects an (unlikely high) 50% change in $R_{\rm eff}$ with respect to the actual measurement and translates into a 10–20% shift of the $\gamma_{\rm DM} - f_{\rm b}$ relation. This is comparable to the width of the coloured areas in Fig. 8. Because our true measurement error on $R_{\rm eff}$ is certainly much better than 50%, we conclude that this parameter does not affect the models much, given the accuracy of the observations.

6. Towards H_0 with HE 0435-1223

The `gravlens` software (Keeton 2004) was used in combination with the dynamical and stellar population constraints to

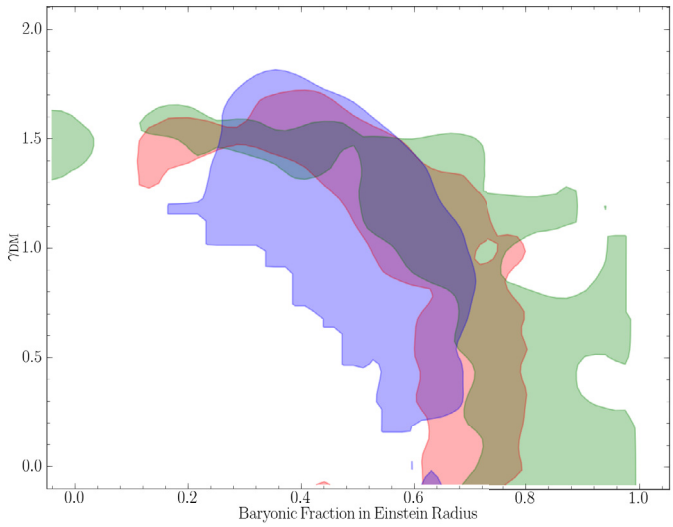

Fig. 8. Effet of a change in $R_{\rm eff}$ on the $\gamma_{\rm DM} - f_{\rm b}$ relation. The contours show the region containing 68% of the models. The value adopted in this paper is $R_{\rm eff} = 8.44$ kpc, as measured from HST images. This corresponds to the area in red. The models in the blue region have $R_{\rm eff} = 4.22$ kpc, and the region in green has $R_{\rm eff} = 12.88$ kpc.

reproduce the lensing configuration of the quasar images and to attempt converting the time delays into H_0. We adopted a total potential well composed of the main lensing galaxy, the nearby galaxy G22 (see Morgan et al. 2005) plus an external shear.

The main galaxy is composed of a projected Hernquist + cuspy halo model identical to those in Eqs. (1) and (2).

For the Hernquist profile, we fixed the ellipticity and PA of the lensing galaxy to the observed ones.

We then estimated how well each of the models described in Sect. 5.2 reproduces the observed image configuration. In doing this, we allowed only the external shear (γ, θ_γ), the Einstein radius of G22 and H_0 to vary. The potential well of G22 was assumed to lie at its observed position and was modelled as a singular isothermal sphere (SIS). We assumed a conservative value of $R_{\rm E}({\rm G22}) < 0\farcs4$, following the results of Morgan et al. (2005), who have found $R_{\rm E}({\rm G22}) = 0\farcs18$.

We show in Fig. 9 the value of H_0 for each lens model as a function of its dark matter slope, $\gamma_{\rm DM}$. The colour code in the figure corresponds to the value of $\chi^2_{\rm Tot}$, where the baryonic fraction, $f_{\rm b} \pm \sigma(f_{\rm b})$, in the Einstein radius is now included in the calculation:

$$\chi^2_{\rm Tot} = \chi^2_{\rm Jeans} + \left(\frac{f_{\rm b}({\rm model}) - f_{\rm b}({\rm obs})}{\sigma(f_{\rm b})}\right)^2. \quad (7)$$

Including $f_{\rm b}$ is justified by Fig. 6, showing that different values of $f_{\rm b}$ select different lens models. We display our results for the two most common IMFs in use in stellar population modelling, the Salpeter and the Kroupa IMFs.

The points define a $\chi^2_{\rm Tot}$ surface with a clear valley which minimum indicates the best dark matter slopes for each IMF. These are $\gamma_{\rm DM}({\rm Sal}) \sim 1.15$ and $\gamma_{\rm DM}({\rm Kro}) \sim 1.54$ for the Salpeter and the Kroupa IMFs, respectively. Each model shown in Fig. 9 is also required to display a good lensing chi-square, $\chi^2_{\rm L}$, after fitting of the quasar image positions with `gravlens`. The values of $\chi^2_{\rm L}$ are systematically lower for the lensing galaxies with Kroupa IMFs. The present lensing and dynamical work therefore favours a lensing galaxy with a Kroupa IMF, as also found by Cappellari et al. (2006) from 3D spectroscopy of early-type galaxies and by Ferreras et al. (2008) using the SLACS sample of strong lenses (Bolton et al. 2008).

The points in Fig. 9 all have $\chi^2_{\rm Jeans} < 1$, which prevents us, for now, from giving a value for H_0 given the observational uncertainty on $f_{\rm b}$ and $\sigma_{\rm ap}$. The measurement errors on both parameters will, however, easily improve with deeper and higher resolution spectroscopy of the lens.

With the current observational constraints we rely on previous work done on the total mass slope, γ', of lensing galaxies. Koopmans et al. (2009) have measured the probability distribution function of γ' in the SLACS sample of strong lenses. They have found $\langle\gamma'\rangle = 2.085^{+0.025}_{-0.018}$, with an intrinsic spread of $\sigma(\gamma') = 0.20$, also confirmed in a more recent study by Auger et al. (2010). The models with the best $\chi^2_{\rm Tot}$ values in Fig. 9 correspond to a total slope of $\gamma' = 2.1 \pm 0.1$ independent of the choice of an IMF. This is well within the rms limits of Koopmans et al. (2009) and leads to $57 < H_0 < 71$ km s^{-1} Mpc^{-1} with all models equiprobable within this range.

In our analysis we modelled the environment of the lensing galaxy as a SIS that represents galaxy G22, plus an external shear with a PA of the order of $-15°$, and amplitudes in the range $0.06 < \gamma < 0.08$. However, we did not explicitly account for the fact that HE 0435-1223 lies within a group of galaxies (Momcheva 2009). The unkown convergence, κ, associated with the group leads to an overestimate of H_0 by a factor $(1-\kappa)^{-1}$, meaning that the range of acceptable H_0 values would decrease further if we have underestimated the convergence caused by the group. Current imaging data suggest, however, that the line of sight is in fact sightly under-dense compared with other lensed systems (Fassnacht et al. 2011). However, the missing convergence is about $\kappa \sim 0.01$–0.02, leading to at most a 2% change (upwards) in H_0. The above statement should, however, be considered with care because the effect of a group is poorly approximated by a simple convergence term. Explicit modelling of the group halo is likely needed to properly account for the modifications induced on the main lens potential. Deep X-ray and/or optical integral field spectroscopy may turn out to be very useful as well in determining the centroid and mass of the group that contains the galaxy lensing HE 0435-1223.

7. Conclusion

We presented seven years of optical monitoring for the four lensed quasar images of HE 0435-1223. We found that the time delays are better expressed with respect to component B, which is the least affected by stellar microlensing in the lensing galaxy. The formal error bars on the time delays are between 5% and 10% depending on the component, which is remarkable given the very short time delays involved. In addition, the delays are robust against different tests performed on the data, including removal of subsets of data and monte carlo simulations. These tests are possible only with very long light curves, as provided by COSMOGRAIL. Most past lens monitorings have two to three seasons and much coarser temporal sampling. The delays are also independent of the way the microlensing variations are modelled. Given the short length of the delays, additionally improving the error bars will only be possible by increasing the temporal sampling of the curves, i.e., by merging all existing data on HE 0435-1223 taken by different groups over the years.

We introduced a method to convert the time delays into H_0 purely based on external constraints on the radial mass slope of the lens. These constraints come from deep optical spectroscopy of the lens, which allowed us to measure its velocity dispersion and its stellar mass-to-light ratio. The present paper describes

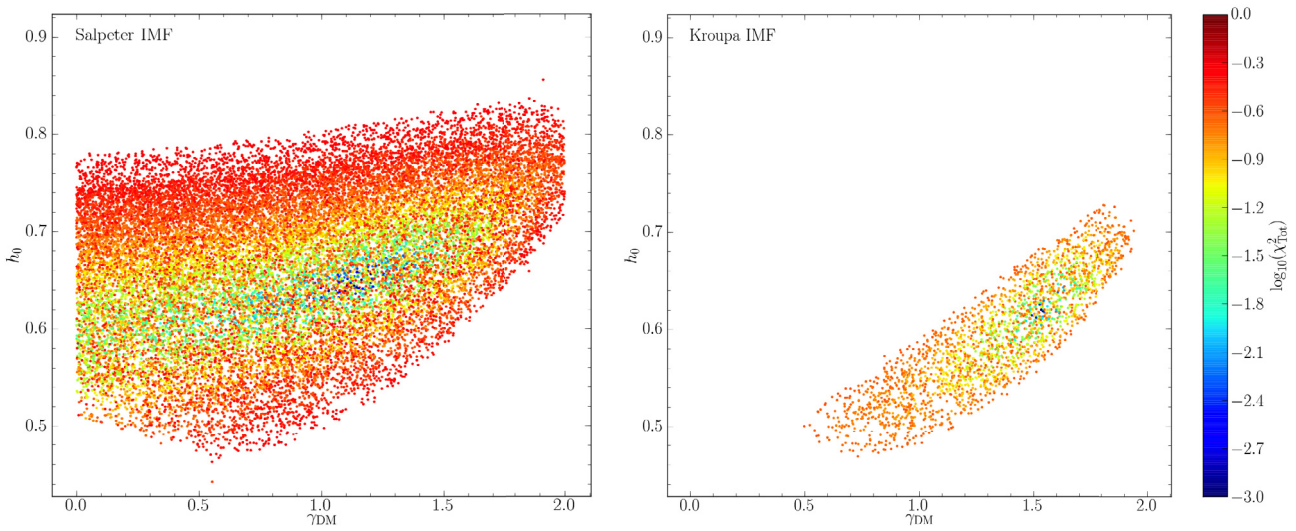

Fig. 9. Distribution of our lens models as a function of the dark matter slope and H_0. The colour code gives the value of $\chi^2_{\rm Tot}$ (see text; Eq. (7)). Only the models with $\chi^2_{\rm Tot} < 1$ are shown. The results in *the left panel* are for a Salpeter IMF, and for a Kroupa IMF in *the right panel*. The lensing χ^2 itself is not included in the figure. However, it is systematically lower for galaxies with Kroupa IMFs than for galaxies with Salpeter IMFs.

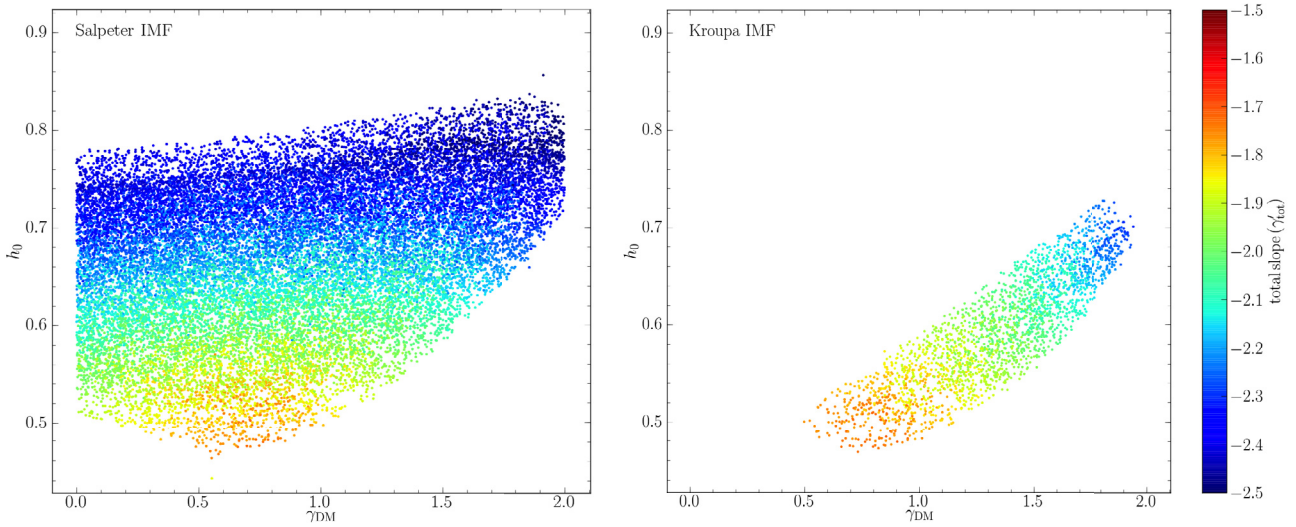

Fig. 10. Same as Fig. 9, but the colour code now gives the slope of the total (dark+luminous) mass profile, γ'. A logarithmic slope of $\gamma' = 2$ corresponds to an isothermal profile, shown in green.

our approach, but the current observations of the lensing galaxy so far lead to a broad range of values for H_0.

Our methodology complement that presented by Suyu et al. (2009, 2010) well. Combining the two in the future will require follow-up observations such as (i) deep HST imaging to map the Einstein ring with high signal-to-noise; (ii) deep high resolution spectroscopy of the lens over a broad spectral range to narrow down the uncertainty on its velocity dispersion and stellar mass; (iii) integral field spectroscopy to measure all redshifts within 30−60″ around the lens; and (iv) X-ray imaging to pinpoint massive groups along the line of sight.

If all these observations are taken for HE 0435-1223 as well as for a few lenses with well measured time delays, the cost in terms of follow-up observations will still remain very modest compared with other existing methods to measure H_0, such as Cepheids and supernovae.

Acknowledgements. We are grateful to all the observers who contributed to the data acquisition at the Euler and Mercator telescopes as well as at Maidanak Observatory. COSMOGRAIL is financially supported by the Swiss National Science Foundation (SNSF). This work is also supported by the Belgian Federal Science Policy (BELSPO) in the framework of the PRODEX Experiment Arrangement C-90312. V.C. thanks the Belgian National Fund for Scientific Research (FNRS). D.S. acknowledges a fellowship from the Alexander von Humboldt Foundation. M.K. has been supported by the Programa Nacional de Astronomía y Astrofísica of the Spanish Ministry of Science and Innovation under grant *AYA2007-67752-C03-01* and DO02-85/2008 from Bulgarian Scientific Research Fund.

References

Auger, M. W., Treu, T., Bolton, A. S., et al. 2010, ApJ, 724, 511
Barnes, J., & Hut, P. 1986, Nature, 324, 446
Binney, J., & Merrifield, M. 1998, Galactic astronomy (Princeton University Press), Princeton Series in Astrophysics
Blackburne, J. A., & Kochanek, C. S. 2010, ApJ, 718, 1079
Bolton, A. S., Burles, S., Koopmans, L. V. E., et al. 2008, ApJ, 682, 964
Burud, I., Hjorth, J., Jaunsen, A. O., et al. 2000, ApJ, 544, 117
Burud, I., Courbin, F., Magain, P., et al. 2002, A&A, 383, 71
Cappellari, M., Bacon, R., Bureau, M., et al. 2006, MNRAS, 366, 1126
Chantry, V., & Magain, P. 2007, A&A, 470, 467
Chantry, V., Sluse, D., & Magain, P. 2010, A&A, 522, A95
Eigenbrod, A., Courbin, F., Meylan, G., Vuissoz, C., & Magain, P. 2006, A&A, 451, 759

Fassnacht, C. D., Xanthopoulos, E., Koopmans, L. V. E., & Rusin, D. 2002, ApJ, 581, 823
Fassnacht, C. D., Koopmans, L. V. E., & Wong, K. C. 2011, MNRAS, 410, 2167
Ferreras, I., Saha, P., & Burles, S. 2008, MNRAS, 383, 857
Freedman, W. L., & Madore, B. F. 2010, ARA&A, 48, 673
Frieman, J. A., Turner, M. S., & Huterer, D. 2008, ARA&A, 46, 385
Gillon, M., Magain, P., Chantry, V., et al. 2007a, in Transiting Extrapolar Planets Workshop, ed. C. Afonso, D. Weldrake, & T. Henning, ASP Conf. Ser., 366, 113
Gillon, M., Pont, F., Moutou, C., et al. 2007b, A&A, 466, 743
Goicoechea, L. J. 2002, MNRAS, 334, 905
Hernquist, L. 1990, ApJ, 356, 359
Hu, W. 2005, in Observing Dark Energy, ed. S. C. Wolff & T. R. Lauer, ASP Conf. Ser., 339, 215
Keeton, C. 2004, Gravlens 1.06, Software for Gravitational Lensing: Handbook Version 9
Kochanek, C. S., Morgan, N. D., Falco, E. E., et al. 2006, ApJ, 640, 47
Koleva, M., Prugniel, P., & De Rijcke, S. 2008, Astron. Nachr., 329, 968
Koleva, M., Prugniel, P., Bouchard, A., & Wu, Y. 2009, A&A, 501, 1269
Koopmans, L. V. E., & Treu, T. 2002, ApJ, 568, L5
Koopmans, L. V. E., Bolton, A., Treu, T., et al. 2009, ApJ, 703, L51
Krist, J., & Hook, R. 2004, The Tiny Tim User's Guide Version 6.3
Kroupa, P. 2001, MNRAS, 322, 231
Le Borgne, D., Rocca-Volmerange, B., Prugniel, P., et al. 2004, A&A, 425, 881
Letawe, Y., Magain, P., Letawe, G., Courbin, F., & Hutsemékers, D. 2008, ApJ, 679, 967
Magain, P., Courbin, F., & Sohy, S. 1998, ApJ, 494, 472
Magain, P., Courbin, F., Gillon, M., et al. 2007, A&A, 461, 373
Momcheva, I. G. 2009, Ph.D. Thesis, The University of Arizona
Morgan, N. D., Kochanek, C. S., Pevunova, O., & Schechter, P. L. 2005, AJ, 129, 2531
Mosquera, A. M., Muñoz, J. A., Mediavilla, E., & Kochanek, C. S. 2011, ApJ, 728, 145
Navarro, J. F., Frenk, C. S., & White, S. D. M. 1996, ApJ, 462, 563
Pelt, J., Kayser, R., Refsdal, S., & Schramm, T. 1996, A&A, 305, 97
Prugniel, P., & Soubiran, C. 2001, A&A, 369, 1048
Prugniel, P., Soubiran, C., Koleva, M., & Le Borgne, D. 2007 [arXiv:0703658]
Refsdal, S. 1964, MNRAS, 128, 307
Riess, A. G., Macri, L., Casertano, S., et al. 2009, ApJ, 699, 539
Riess, A. G., Macri, L., Casertano, S., et al. 2011, ApJ, 730, 119
Salpeter, E. E. 1955, ApJ, 121, 161
Schlegel, D. J., Finkbeiner, D. P., & Davis, M. 1998, ApJ, 500, 525
Suyu, S. H., Marshall, P. J., Blandford, R. D., et al. 2009, ApJ, 691, 277
Suyu, S. H., Marshall, P. J., Auger, M. W., et al. 2010, ApJ, 711, 201
van Dokkum, P. G. 2001, PASP, 113, 1420
Vuissoz, C., Courbin, F., Sluse, D., et al. 2007, A&A, 464, 845
Vuissoz, C., Courbin, F., Sluse, D., et al. 2008, A&A, 488, 481
Warren, S. J., & Dye, S. 2003, ApJ, 590, 673
Wisotzki, L., Christlieb, N., Bade, N., et al. 2000, A&A, 358, 77
Wisotzki, L., Schechter, P. L., Bradt, H. V., Heinmüller, J., & Reimers, D. 2002, A&A, 395, 17